Supporting Information

Dinuclear Lanthanide Molecular Magnetic Material Bridged by Tetrazine Derivatives Containing N6 and N8 Atom Sites Display Slow Magnetic Relaxation Behavior

Ji-Tun Chen,[a] Rui Guo,[a] Yi-Quan Zhang*[b] and Wen-Bin Sun,*[a]

a. Key Laboratory of Functional Inorganic Material Chemistry Ministry of Education, School of Chemistry and Material Science Heilongjiang University, 74 Xuefu Road, Harbin 150080, P. R. China.
E-mail: wenbinsun@126.com

b. Jiangsu Key Laboratory for NSLSCS, School of Physical Science and Technology, Nanjing Normal University, Nanjing 210023, P. R. China.
E-mail: zhangyiquan@njnu.edu.cn

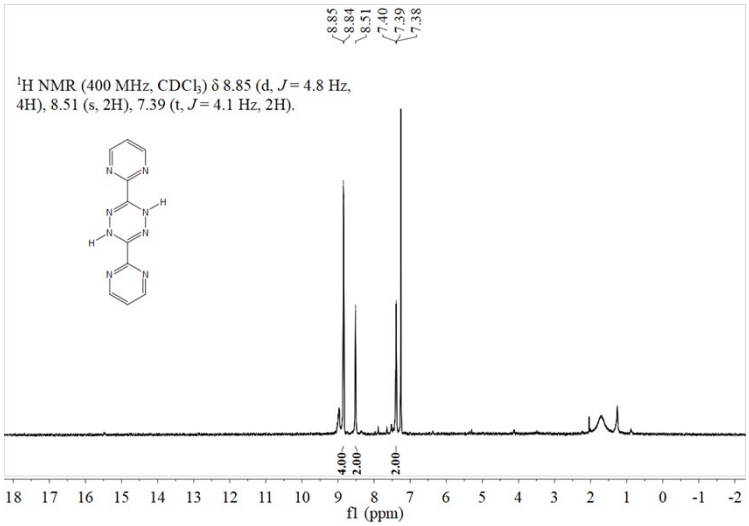

Fig. S1. 1H NMR spectrum of H_2bmtz.

Table S1. Crystallographic data for **1**-**3**.

Complex	**1**	**2**	**3**
Empirical formula	$C_{62}H_{36}Cl_4Dy_2F_{18}N_6O_{12}S_6$	$C_{29}H_{16}DyF_9N_4O_6S_3$	$C_{40}H_{18}Dy_2F_{36}N_8O_{14}$
FW (g mol^{-1})	2058.13	945.13	1843.62
Crystal system	orthorhombic	monoclinic	triclinic
Space group	*Pccn*	*C2/c*	*P-1*
Temperature (K)	297	293	293
a (Å)	24.4222	32.874	12.3888
b (Å)	22.5632	10.419	13.7920
c (Å)	13.7569	19.990	18.7166
α (°)	90	90	88.227
β (°)	90	97.14	86.765
γ (°)	90	90	74.619
V (Å^3)	7580.6(3)	6793.8	3078.2
ρ_{cacd} (Mg.m^{-3})	1.803	1.848	1.989
μ (mm^{-1})	2.368	14.393	14.462
F (000)	4016.0	3680.0	1764.0
Independent relections	7855	6046	10861
Rint	0.0333	0.1363	0.0993
R1 [I > 2σ(I)]	0.0384	0.0964	0.0738
wR2 (all data)	0.0893	0.2719	0.1880
Goodness of fit on F^2	1.078	0.987	0.988
CCDC numbers	2306039	2306040	2306041

Table S2. Selected bond lengths (Å) and angles (°) for **1**.

Dy1-O1	2.280(3)	Dy1-O5	2.305(3)
Dy1-O2	2.316(3)	Dy1-O6	2.329(3)
Dy1-O3	2.339(3)	Dy1-N1	2.650(3)
Dy1-O4	2.285(3)	Dy1-N3	2.555(4)
O1-Dy1-O2	73.81(12)	O5-Dy1-O2	78.87(13)
O1-Dy1-O3	77.61(12)	O5-Dy1-O3	139.42(12)
O1-Dy1-O4	108.68(13)	O5-Dy1-O6	73.64(12)
O1-Dy1-O5	83.83(12)	O5-Dy1-N1	67.76(11)
O1-Dy1-O6	147.50(12)	O5-Dy1-N3	99.01(12)
O1-Dy1-N1	77.00(11)	O6-Dy1-O3	134.30(12)
O1-Dy1-N3	133.43(12)	O6-Dy1-N1	113.93(12)
O2-Dy1-O3	128.06(13)	O6-Dy1-N3	74.29(12)
O2-Dy1-O6	79.00(12)	N3-Dy1-N1	61.97(11)
O2-Dy1-N1	137.47(12)	C5-O1-Dy1	135.9(3)
O2-Dy1-N3	152.62(13)	C7-O2-Dy1	131.5(3)
O3-Dy1-N1	73.01(12)	C13-O3-Dy1	136.8(3)
O3-Dy1-N3	70.42(13)	C15-O4-Dy1	133.4(3)
O4-Dy1-O2	76.29(12)	C21-O5-Dy1	136.6(3)
O4-Dy1-O3	73.11(12)	C23-O6-Dy1	132.2(4)
O4-Dy1-O5	147.46(12)	N21-N1-Dy1	121.3(3)
O4-Dy1-O6	81.22(13)	C25-N1-Dy1	119.9(3)
O4-Dy1-N1	143.36(12)	C26-N3-Dy1	123.9(3)
O4-Dy1-N3	93.60(12)	C30-N3-Dy1	117.5(3)

Table S3. Selected bond lengths (Å) and angles (°) for **2**.

Dy1-O1	2.318(12)	Dy1-O5	2.269(11)
Dy1-O2	2.265(13)	Dy1-O6	2.333(11)
Dy1-O3	2.290(12)	Dy1-N3	2.626(13)
Dy1-O4	2.323(12)	Dy1-N1	2.528(15)
O1-Dy1-N3	81.4(5)	O5-Dy1-O3	132.3(5)
O1-Dy1-N1	143.4(6)	O5-Dy1-O4	150.2(6)
O2-Dy1-O1	72.8(5)	O5-Dy1-O6	71.8(5)
O2-Dy1-O3	98.2(6)	O5-Dy1-N3	70.1(5)
O2-Dy1-O4	77.3(6)	O5-Dy1-N1	89.9(6)
O2-Dy1-O5	107.4(6)	O6-Dy1-O1	127.2(5)

O2-Dy1-O6	81.1(6)	O6-Dy1-N3	120.8(5)
O2-Dy1-N3	153.5(6)	O6-Dy1-N1	74.4(5)
O2-Dy1-N1	143.8(6)	N1-Dy1-N3	62.1(6)
O3-Dy1-O1	76.7(6)	C5-O1-Dy1	136.0(16)
O3-Dy1-O4	73.8(5)	C7-O2-Dy1	131.9(13)
O3-Dy1-O6	153.4(5)	C13-O3-Dy1	138.4(15)
O3-Dy1-N3	69.2(5)	C15-O4-Dy1	130.3(12)
O3-Dy1-N1	92.5(6)	C21-O5-Dy1	138.4(16)
O4-Dy1-O1	134.0(6)	C23-O6-Dy1	133.2(12)
O4-Dy1-O6	80.2(5)	C25-N3-Dy1	123.9(15)
O4-Dy1-N3	118.6(5)	C28-N3-Dy1	116.8(14)
O4-Dy1-N1	72.7(6)	N2-N1-Dy1	124.5(13)
O5-Dy1-O1	73.5(6)	C29-N1-Dy1	122.7(15)

Table S4. Selected bond lengths (Å) and angles (°) for **3**.

Dy1-N2	2.627(10)	Dy2-N6	2.668(10)
Dy1-N3	2.552(9)	Dy2-N7	2.572(9)
Dy1-O7	2.401(9)	Dy2-O1	2.509(8)
Dy1-O8	2.356(8)	Dy2-O2	2.371(9)
Dy1-O9	2.325(9)	Dy2-O3	2.376(8)
Dy1-O10	2.337(8)	Dy2-O4	2.338(9)
Dy1-O11	2.520(8)	Dy2-O5	2.394(9)
Dy1-O12	2.341(9)	Dy2-O6	2.390(9)
Dy1-O13	2.398(7)	Dy2-O14	2.398(8)
N3-Dy1-N2	62.7(5)	O3-Dy2-N6	147.1(5)
O7-Dy1-N2	100.5(5)	O3-Dy2-N7	135.9(5)
O7-Dy1-N3	66.1(5)	O3-Dy2-O1	68.2(4)
O7-Dy1-O11	133.1(4)	O3-Dy2-O5	77.3(5)
O8-Dy1-N2	70.0(5)	O3-Dy2-O6	76.0(5)
O8-Dy1-N3	105.5(5)	O3-Dy2-O14	86.1(4)
O8-Dy1-O7	70.5(4)	O4-Dy2-N6	133.8(4)
O8-Dy1-O11	127.9(4)	O4-Dy2-N7	72.5(4)
O8-Dy1-O13	68.1(4)	O4-Dy2-O1	73.3(4)
O9-Dy1-N2	147.0(5)	O4-Dy2-O2	80.8(5)
O9-Dy1-N3	135.7(5)	O4-Dy2-O3	75.1(5)
O9-Dy1-O7	74.2(5)	O4-Dy2-O5	137.1(5)

O9-Dy1-O8	77.7(5)	O4-Dy2-O6	71.1(5)
O9-Dy1-O11	70.2(4)	O4-Dy2-O14	141.7(4)
O9-Dy1-O12	136.6(4)	O5-Dy2-N6	70.1(5)
O9-Dy1-O13	83.2(4)	O5-Dy2-N7	108.2(5)
O10-Dy1-N2	134.2(4)	O5-Dy2-O1	124.3(5)
O10-Dy1-N3	73.1(4)	O5-Dy2-O14	66.5(4)
O10-Dy1-O7	70.2(4)	O6-Dy2-N6	97.1(5)
O10-Dy1-O8	137.1(5)	O6-Dy2-N7	65.8(5)
O10-Dy1-O9	75.7(4)	O6-Dy2-O1	134.6(4)
O10-Dy1-O11	72.0(4)	O6-Dy2-O5	70.8(5)
O10-Dy1-O12	80.8(4)	O6-Dy2-O14	136.4(4)
O10-Dy1-O13	139.4(4)	O14-Dy2-N6	76.9(4)
O11-Dy1-N2	125.9(5)	O14-Dy2-N7	137.1(4)
O11-Dy1-N3	126.2(4)	O14-Dy2-O1	68.7(4)
O12-Dy1-N2	71.8(5)	C18-N2-Dy1	127.3(13)
O12-Dy1-N3	66.9(5)	C19-N2-Dy1	118.3(11)
O12-Dy1-O7	130.0(4)	N4-N3-Dy1	125.1(10)
O12-Dy1-O8	139.6(4)	C20-N3-Dy1	123.3(12)
O12-Dy1-O11	68.1(4)	C22-N6-Dy2	117.4(12)
O12-Dy1-O13	92.1(4)	C25-N6-Dy2	126.0(12)
O13-Dy1-N2	78.6(4)	N8-N7-Dy2	124.6(10)
O13-Dy1-N3	139.9(5)	C21-N7-Dy2	122.8(12)
O13-Dy1-O7	136.0(4)	C4-O1-Dy2	130.4(12)
O13-Dy1-O11	68.2(4)	C2-O2-Dy2	128.7(14)
N7-Dy2-N6	62.3(5)	C9-O3-Dy2	132.6(14)
O1-Dy2-N6	128.0(4)	C7-O4-Dy2	133.0(14)
O1-Dy2-N7	127.1(4)	C12-O5-Dy2	132.6(14)
O2-Dy2-N6	73.8(5)	C14-O6-Dy2	137.1(14)
O2-Dy2-N7	66.9(4)	C29-O7-Dy1	133.7(13)
O2-Dy2-O1	68.7(4)	C27-O8-Dy1	139.2(13)
O2-Dy2-O3	135.0(4)	C32-O9-Dy1	130.7(13)
O2-Dy2-O5	140.4(5)	C34-O10-Dy1	132.6(13)
O2-Dy2-O6	130.2(5)	C37-O11-Dy1	128.4(12)
O2-Dy2-O14	90.2(4)	C39-O12-Dy1	132.2(13)

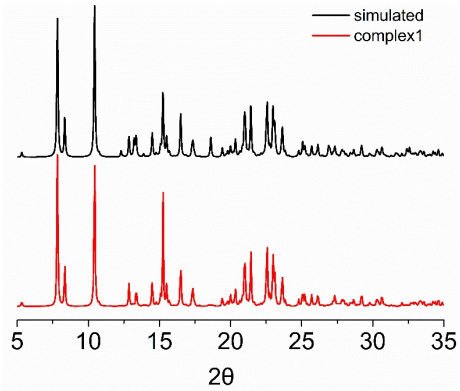

Fig. S2. PXRD analysis of complex **1**. The black line is simulated data from single crystal data.

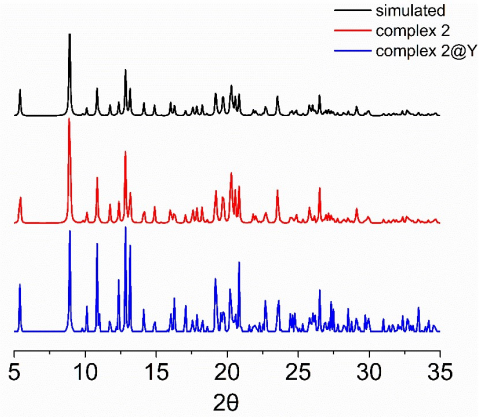

Fig. S3. PXRD analysis of complex **2** and **2@Y**. The black line is simulated data from single crystal data.

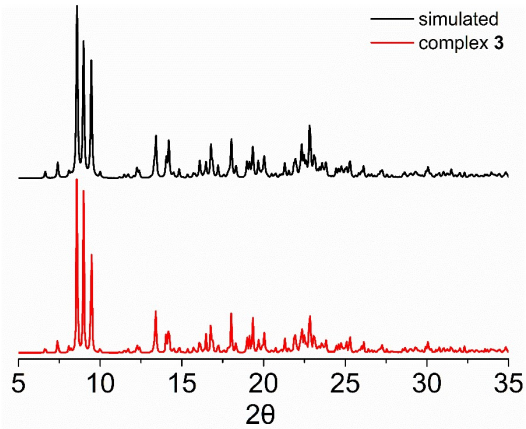

Fig. S4. PXRD analysis of complex **3**. The black line is simulated data from single crystal data.

Table S5. Continuous Shape Measures (CShMs) of the coordination geometry for Dy^{III} ion in compounds **1**–**3** (S values calculated with the Shape program). The S values indicated the proximity to the ideal polyhedron, thus, *S* = 0 corresponds to the non-distorted polyhedron. The three closer ideal geometries to the real complexes are listed and below are the symmetry and description for each polyhedron.

Complexes		s	polyhedron
1	Dy1	0.988	TDD-8, D_{2d}, Triangular dodecahedron
		1.322	SAPR-8, D_{4d}, Square antiprism
		2.267	BTPR-8, C_{2v}, Biaugmented trigonal prism
2	Dy1	0.532	TDD-8, D_{2d}, Triangular dodecahedron
		2.542	SAPR-8, D_{4d}, Square antiprism
		2.594	BTPR-8, C_{2v}, Biaugmented trigonal prism
3	Dy1	0.541	CSAPR-9, C_{4v} Spherical capped square antiprism
		0.994	MFF-9, Cs Muffin
		1.161	JCSAPR-9, C_{4v} Capped square antiprism J10
	Dy2	0.612	CSAPR-9, C_{4v} Spherical capped square antiprism
		0.965	MFF-9, Cs Muffin
		1.308	JCSAPR-9, C_{4v} Capped square antiprism J10

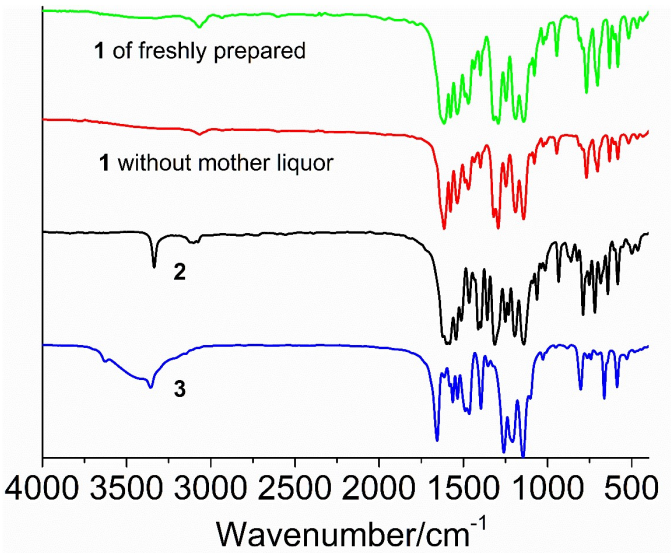

Fig. S5. The IR spectrum of **1**, **2** and **3**.

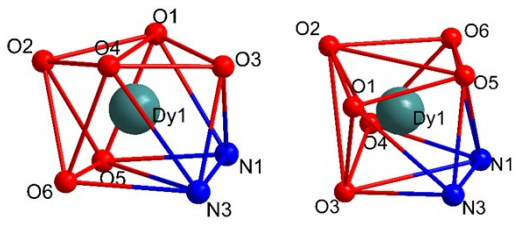

Fig. S6. The local coordination of complexes **1** (left) and **2** (right).

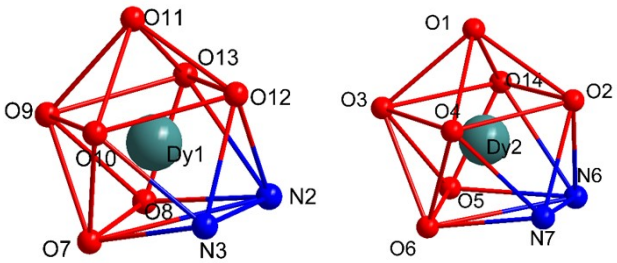

Fig. S7. The local coordination of complex **3**.

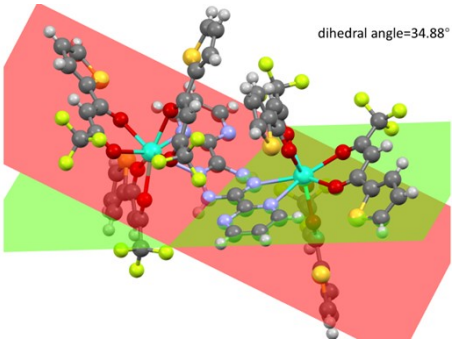

Fig. S8. The dihedral angle of the two opening rings of the H_2bmtz ligand in complex **2**.

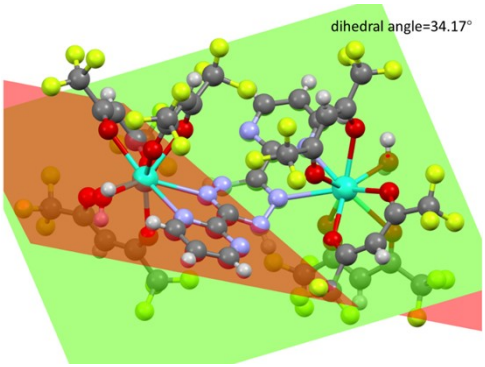

Fig. S9. The dihedral angle of the two opening rings of the H_2bmtz ligand in complex **3**.

Table S6. the intramolecular and nearest intermolecular Dy···Dy distance for **1**-**3**.

Complex	the intramolecular Dy···Dy distance(Å)	the nearest intermolecular Dy···Dy distance(Å)
1	7.985	9.156
2	7.460	10.019
3	7.683	6.177

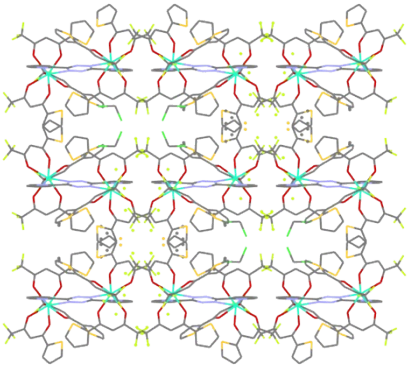

Fig. S10. The packing structure of complex **1**.

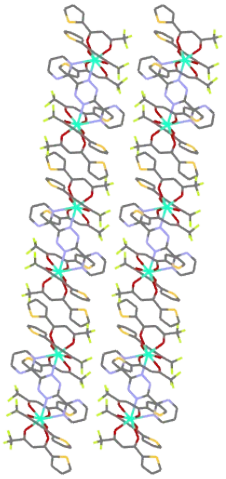

Fig. S11. The packing structure of complex **2**.

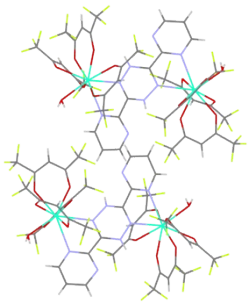

Fig. S12. The packing structure of complex **3**.

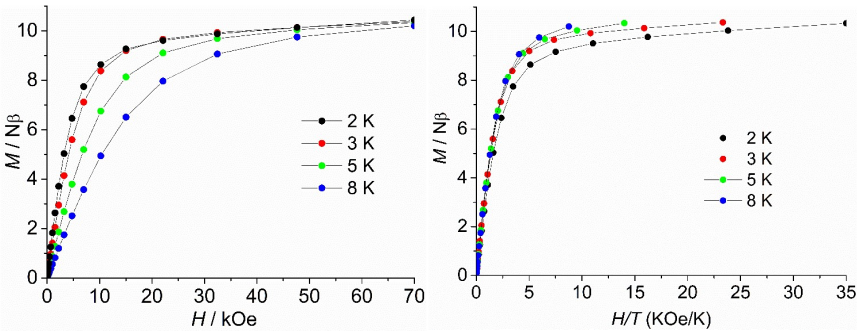

Fig. S13. Field dependence of the magnetization between 2 and 8 K for **1**.

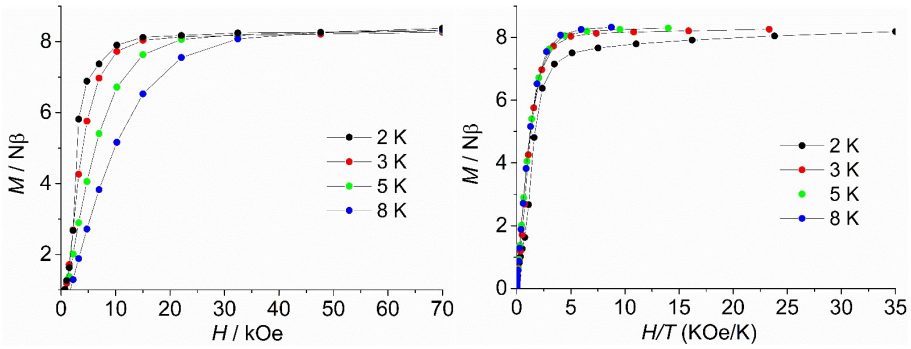

Fig. S14. Field dependence of the magnetization between 2 and 8 K for **2**.

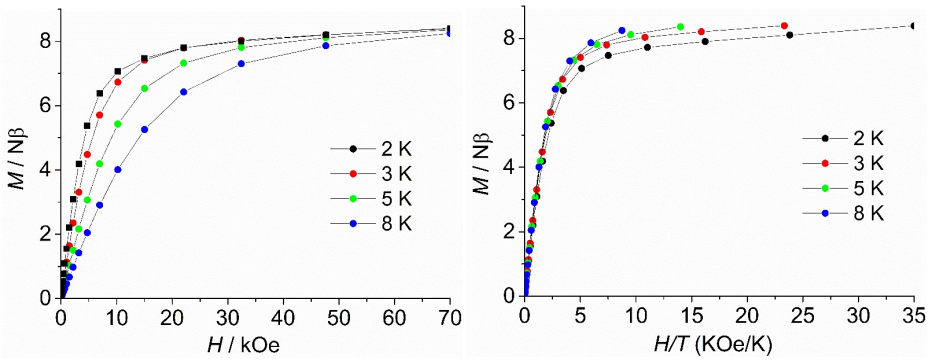

Fig. S15. Field dependence of the magnetization between 2 and 8 K for **3**.

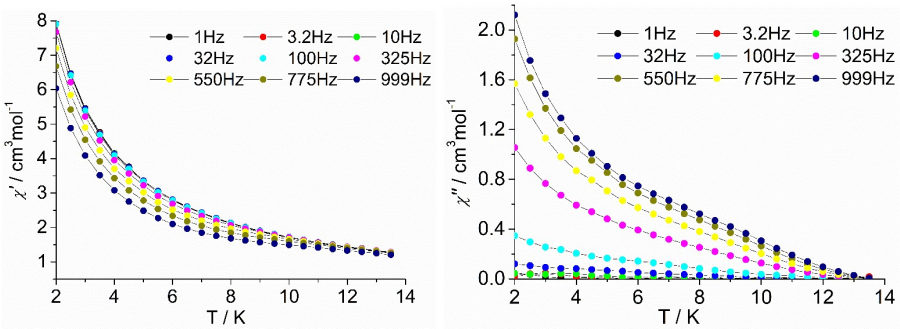

Fig. S16. Temperature dependence of the in-phase (χ') ac susceptibility (left) and temperature dependence of the out-of-phase (χ'') ac susceptibility (right) of complex **1** under zero dc field.

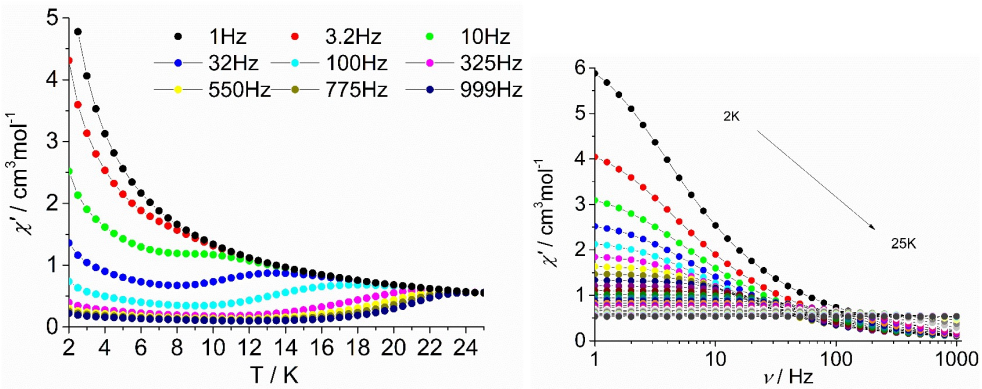

Fig. S17. Temperature dependence of the in-phase (χ') ac susceptibility (left) and frequency dependence of the in-phase (χ') ac susceptibility (right) of complex **2** under zero dc field.

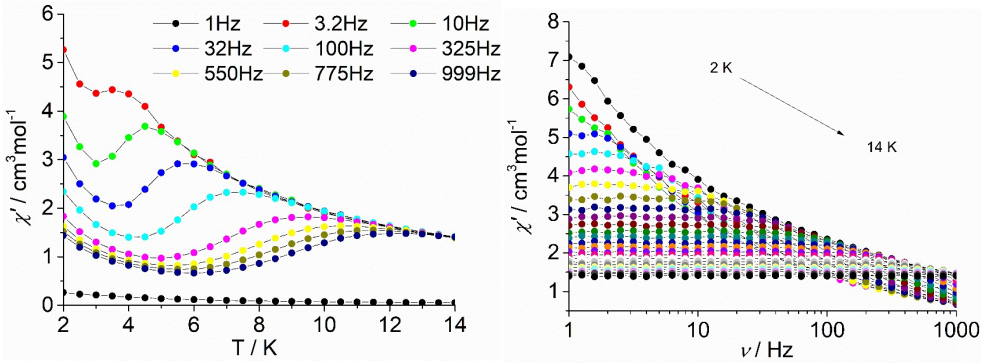

Fig. S18. Temperature dependence of the in-phase (χ') ac susceptibility (left) and frequency dependence of the in-phase (χ') ac susceptibility (right) of complex **3** under zero dc field.

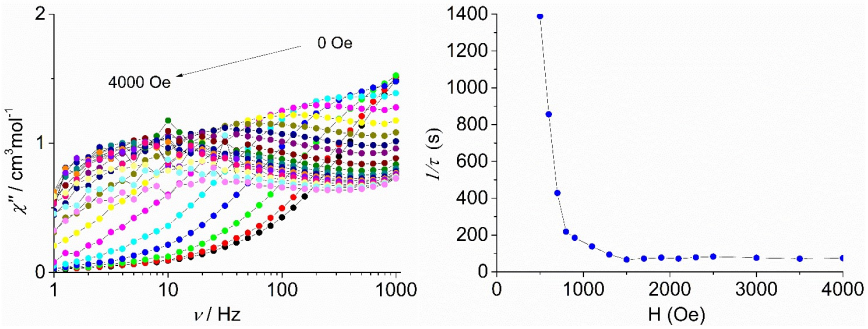

Fig. S19. Plot of the frequency dependence of the out-of-phase (χ'') ac susceptibility component under indicated dc field at 3 K for complex **1** (left). Plot of $1/\tau$ vs. H for **1** under different dc fields at 3 K (right).

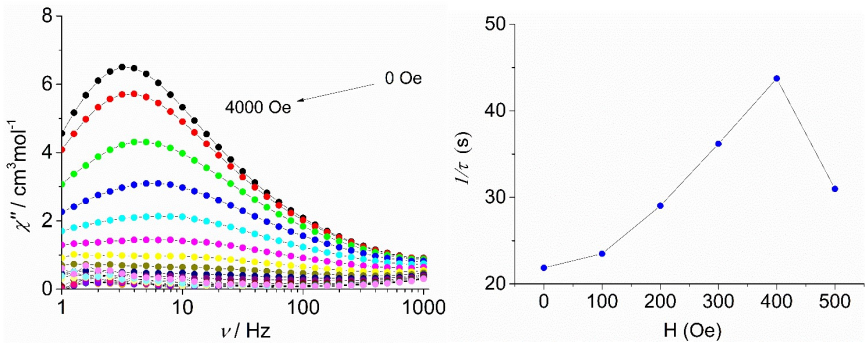

Fig. S20. Plot of the frequency dependence of the out-of-phase (χ'') ac susceptibility component under indicated dc field at 3 K for complex **2** (left). Plot of $1/\tau$ vs. H for **2** under different dc fields at 3 K (right).

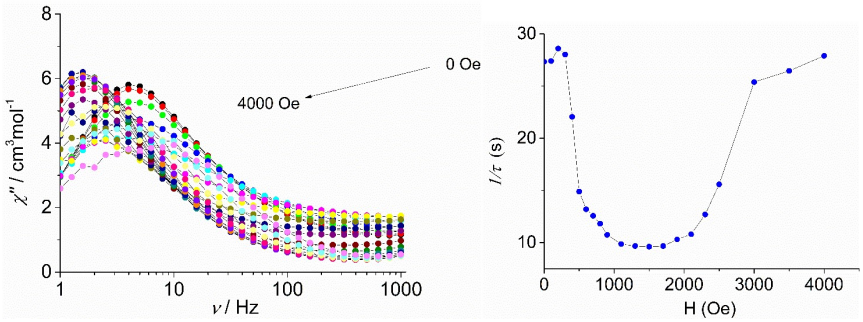

Fig. S21. Plot of the frequency dependence of the out-of-phase (χ'') ac susceptibility component under indicated dc field at 3 K for complex **3** (left). Plot of 1/τ vs. H for **3** under different dc fields at 3 K (right).

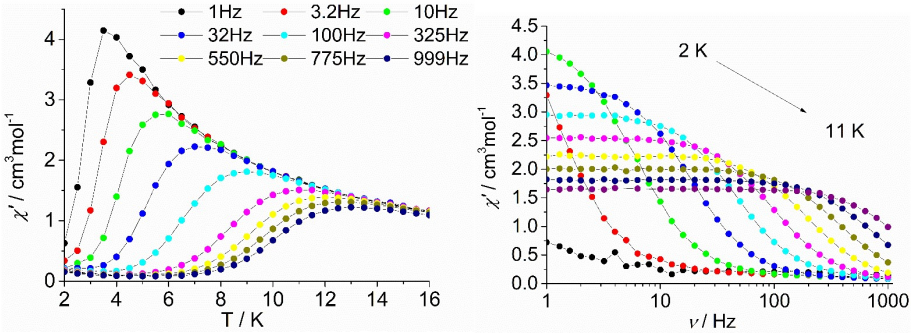

Fig. S22. Temperature dependence of the in-phase (χ') ac susceptibility (left) and frequency dependence of the in-phase (χ') ac susceptibility (right) of complex **1** under 1500 Oe dc field.

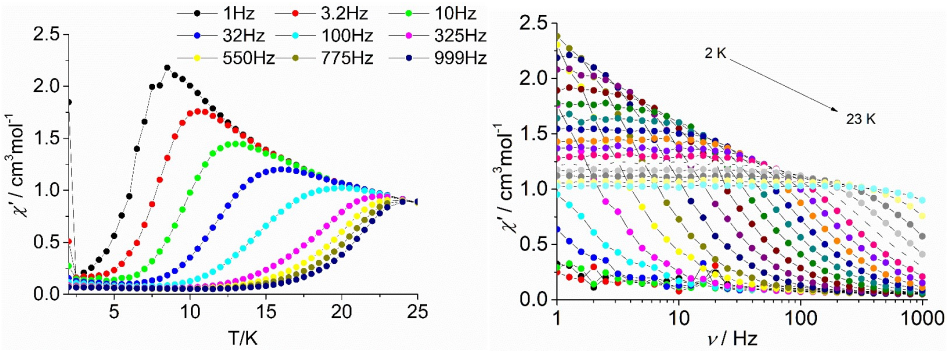

Fig. S23. Temperature dependence of the in-phase (χ') ac susceptibility (left) and frequency dependence of the in-phase (χ') ac susceptibility (right) of complex **2** under 1500 Oe dc field.

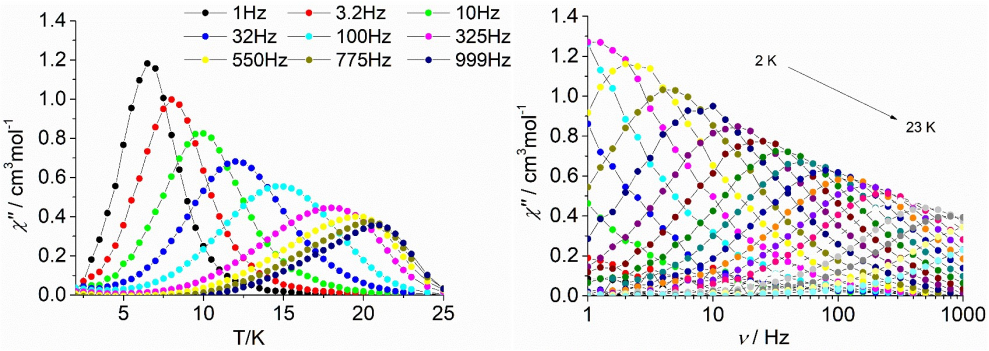

Fig. S24. Temperature dependence of the out-of-phase (χ'') ac susceptibility (left) and frequency dependence of the out-of-phase (χ'') ac susceptibility (right) of complex **2** under 1500 Oe dc field.

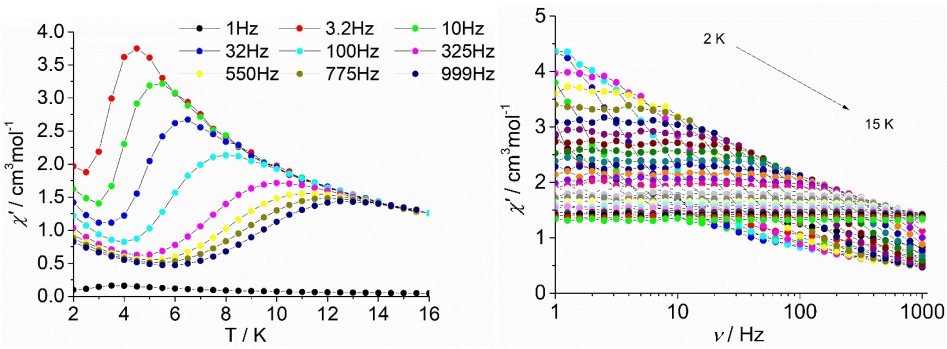

Fig. S25. Temperature dependence of the in-phase (χ') ac susceptibility (left) and frequency dependence of the in-phase (χ') ac susceptibility (right) of complex **3** under 1500 Oe dc field.

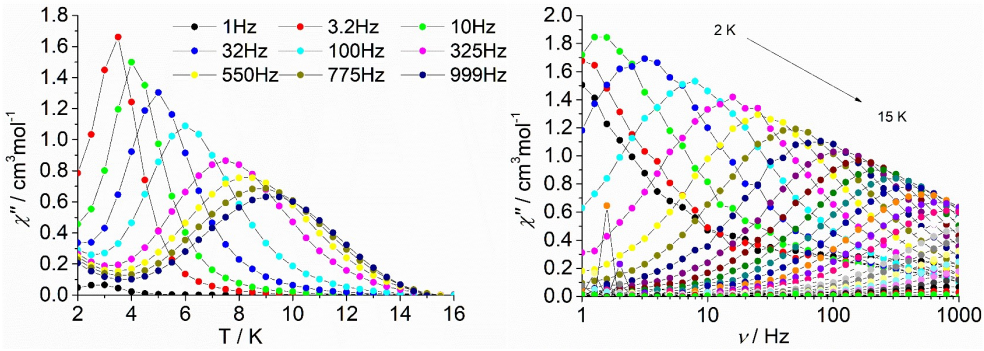

Fig. S26. Temperature dependence of the out-of-phase (χ'') ac susceptibility (left) and frequency dependence of the out-of-phase (χ'') ac susceptibility (right) of complex **3** under 1500 Oe dc field.

Table S7. Energy barriers obtained from the Arrhenius law fitting and Equation 1 of the out-of-phase (χ'') ac susceptibility data under zero field.

Relaxation processes	Raman, QTM and Orbach processes				
	q (s)	C ($s^{-1}\cdot K^{-n}$)	n	U_{eff}/κ_B (K)	τ_0 (s)
2	0.03	0.20	2.80	135(3)	3.74E-7

3	0.23	0.49	3.53	46(7)	1.41E-6
2@Y	0.76	4.69E-4	5.21	142(4)	1.32E-8

Table S8. Energy barriers obtained from the Arrhenius law fitting and Equation 2 of the out-of-phase (χ'') ac susceptibility data under 1500 Oe dc field.

Relaxation processes	Raman and Orbach processes			
	C ($s^{-1}\cdot K^{-n}$)	n	U_{eff}/k_B (K)	τ_0 (s)
1	0.03	5.04	73(3)	2.15E-6
2	1.63E-4	5.51	227(4)	1.40E-8
3	0.04	5.04	62(8)	1.39E-6
2@Y	1.57E-4	5.53	198(1)	9.17E-8

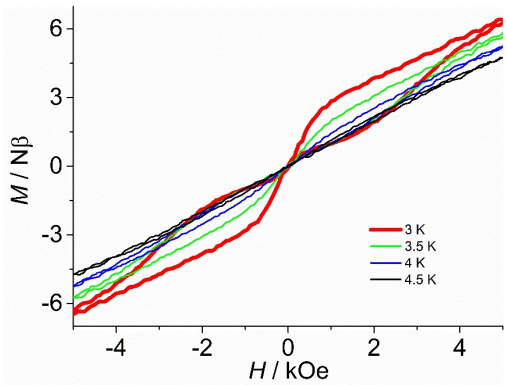

Fig. S27. Field dependence of magnetization of **2** at 50 Oe s^{-1}**.**

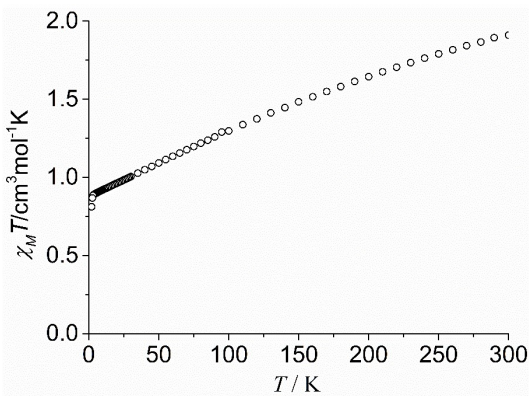

Fig. S28. Temperature dependence of the magnetic susceptibility $\chi_M T$ at 1000 Oe for complexes **2@Y**.

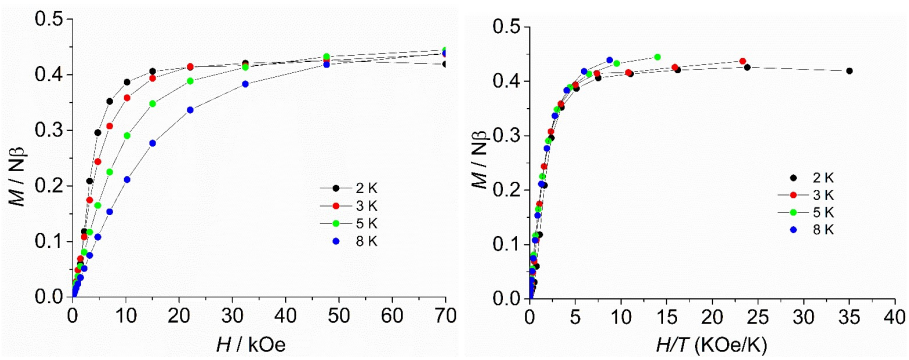

Fig. S29. Field dependence of the magnetization between 2 and 8 K for **2@Y**.

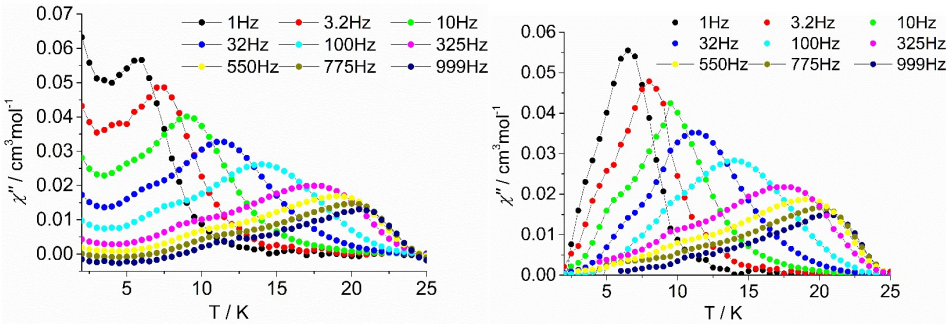

Fig. S30. Temperature dependence of the out-of-phase (χ'') ac susceptibility of complex **2@Y** under zero dc field (left) and 1500 Oe dc field (right).

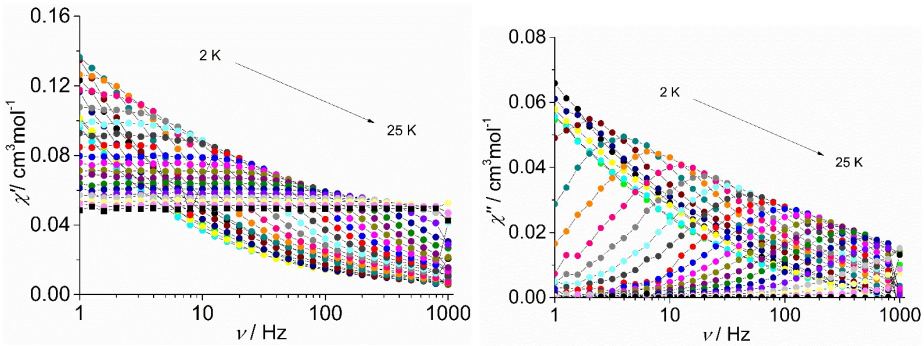

Fig. S31. Frequency dependence of the in-phase (χ') and the out-of-phase (χ'') ac susceptibility (left) of complex **2@Y** under zero dc field.

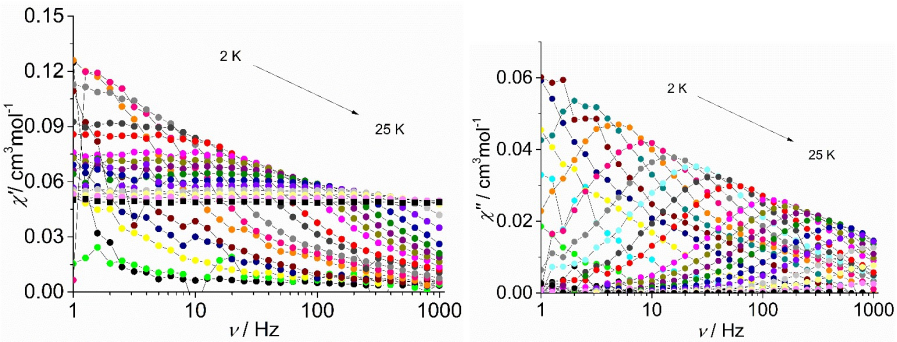

Fig. S32. Frequency dependence of the in-phase (χ') and the out-of-phase (χ'') ac susceptibility (left) of complex **2@Y** under 1500 Oe dc field.

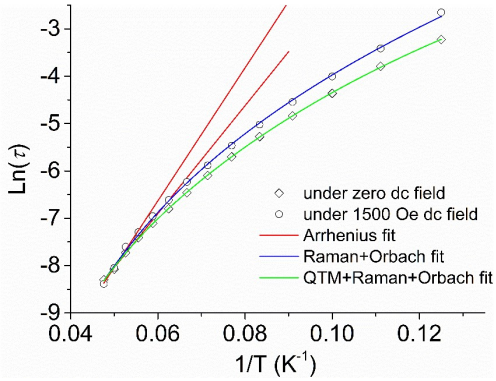

Fig. S33. The ln(τ) vs. T^{-1} plot for complexes **2@Y** on the ac susceptibility data.

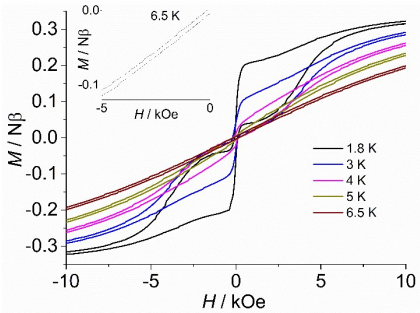

Fig. S34. Field dependence of magnetization of **2@Y** at 200 Oe s^{-1}.

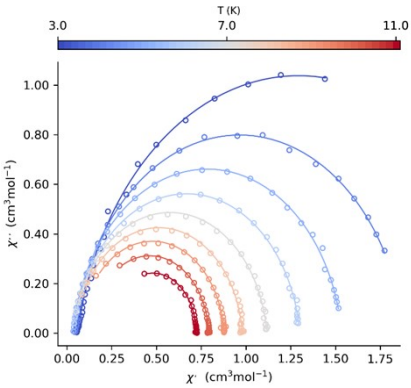

Fig. S35. Cole-Cole (Argand) plot for **1** obtained using the ac susceptibility data. The solid lines correspond to the best fit obtained with a generalized Debye model under 1500 Oe dc field.

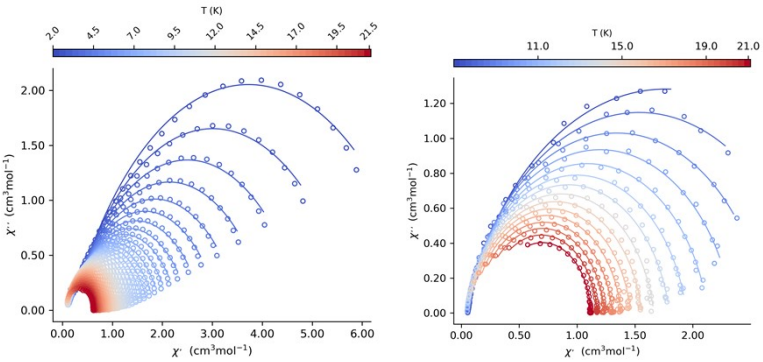

Fig. S36. Cole-Cole (Argand) plot for **2** obtained using the ac susceptibility data. The solid lines correspond to the best fit obtained with a generalized Debye model under zero dc field (left) and 1500 Oe dc field (right).

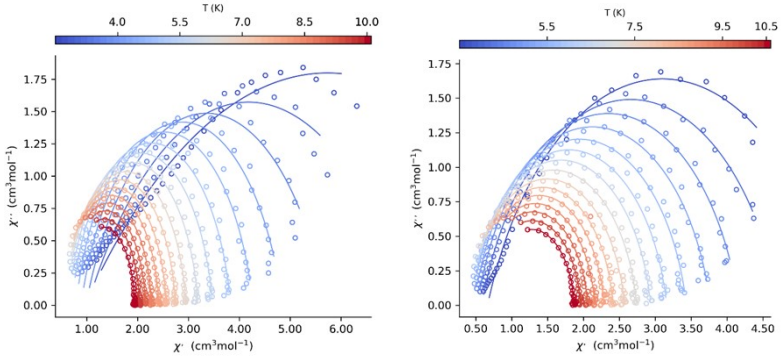

Fig. S37. Cole-Cole (Argand) plot for **3** obtained using the ac susceptibility data. The solid lines correspond to the best fit obtained with a generalized Debye model under zero dc field (left) and 1500 Oe dc field (right).

Table S9. Best fitted parameters (χ_T, χ_S, τ and α) with the extended Debye model for complex **1** at 1500 Oe in the temperature range 3-11 K.

T/ K	χ_S / cm^3 mol^{-1}	χ_T / cm^3 mol^{-1}	τ/s	α
3	0.061	2.525	0.135	0.108
4	0.045	1.882	0.026	0.088
5	0.034	1.534	0.008	0.079
6	0.038	1.300	0.003	0.073
7	0.038	1.116	0.001	0.065
8	0.050	0.978	0.000	0.055
9	0.076	0.877	0.000	0.050
10	0.133	0.792	0.000	0.034
11	0.23	0.721	0.000	0.002

Table S10. Best fitted parameters (χ_T, χ_S, τ and α) with the extended Debye model for complex **2** at 0 Oe in the temperature range 2-21.5 K.

T/ K	χ_S / cm^3 mol^{-1}	χ_T / cm^3 mol^{-1}	τ/s	α
2	0.196	7.251	0.033	0.328
2.5	0.170	5.852	0.030	0.329
3	0.155	4.848	0.027	0.328
3.5	0.140	4.138	0.024	0.327
4	0.135	3.572	0.021	0.322
4.5	0.130	3.166	0.018	0.318
5	0.126	2.838	0.017	0.311
5.5	0.123	2.563	0.015	0.303
6	0.122	2.340	0.014	0.291
6.5	0.122	2.150	0.012	0.276
7	0.122	1.983	0.013	0.258
7.5	0.121	1.843	0.010	0.240
8	0.121	1.719	0.008	0.220
8.5	0.194	1.641	0.007	0.201
9	0.117	1.520	0.006	0.182

9.5	0.114	1.436	0.005	0.165
10	0.111	1.363	0.004	0.153
10.5	0.108	1.289	0.004	0.138
11	0.105	1.229	0.003	0.128
11.5	0.101	1.171	0.003	0.120
12	0.100	1.118	0.002	0.110
12.5	0.098	1.072	0.002	0.103
13	0.097	1.026	0.001	0.096
13.5	0.096	0.986	0.001	0.091
14	0.097	0.951	0.001	0.084
14.5	0.097	0.918	0.001	0.080
15	0.098	0.888	0.001	0.075
15.5	0.101	0.861	0.000	0.070
16	0.105	0.833	0.000	0.066
16.5	0.109	0.807	0.000	0.060
17	0.115	0.784	0.000	0.057
17.5	0.121	0.761	0.000	0.054
18	0.131	0.739	0.000	0.048
18.5	0.141	0.718	0.000	0.042
19	0.151	0.698	0.000	0.038
19.5	0.166	0.680	0.000	0.028
20	0.183	0.662	0.000	0.021
20.5	0.204	0.648	0.000	0.008
21	0.228	0.633	0.000	0.004
21.5	0.249	0.616	0.000	0.006

Table S11. Best fitted parameters (χ_T, χ_S, τ and α) with the extended Debye model for complex **2** at 1500 Oe in the temperature range 7-21 K.

T/ K	χ_S / cm^3 mol^{-1}	χ_T / cm^3 mol^{-1}	τ/s	α
7	0.044	3.487	0.152	0.184
8	0.048	3.026	0.069	0.163
9	0.044	2.640	0.034	0.14
10	0.048	2.348	0.018	0.131
11	0.048	2.131	0.010	0.124
12	0.050	1.945	0.006	0.115
13	0.056	1.797	0.004	0.107
14	0.062	1.663	0.002	0.101
15	0.070	1.558	0.001	0.098
16	0.082	1.463	0.001	0.092
17	0.102	1.379	0.000	0.084
18	0.125	1.306	0.000	0.081
19	0.165	1.236	0.000	0.064
20	0.210	1.173	0.000	0.048
21	0.248	1.116	0.000	0.019

Table S12. Best fitted parameters (χ_T, χ_S, τ and α) with the extended Debye model for complex **3** at 0 Oe in the temperature range 2.5-10 K.

T/ K	χ_S / cm^3 mol^{-1}	χ_T / cm^3 mol^{-1}	τ/s	α
2.5	0.960	10.512	0.128	0.541
3	1.017	7.346	0.042	0.412
3.5	0.984	5.722	0.018	0.286
4	0.891	4.852	0.009	0.208
4.5	0.794	4.270	0.005	0.163
5	0.709	3.832	0.003	0.137
5.5	0.650	3.474	0.002	0.143
6	0.605	3.190	0.001	0.009
6.5	0.572	2.953	0.000	0.008
7	0.565	2.746	0.000	0.007
7.5	0.558	2.563	0.000	0.006
8	0.560	2.417	0.000	0.005
8.5	0.584	2.270	0.000	0.004
9	0.606	2.152	0.000	0.003
9.5	0.656	2.039	0.000	0.002
10	0.701	1.941	0.000	0.001

Table S13. Best fitted parameters (χ_T, χ_S, τ and α) with the extended Debye model for complex **3** at 1500 Oe in the temperature range 3.5-10.5 K.

T/ K	χ_S / cm^3 mol^{-1}	χ_T / cm^3 mol^{-1}	τ/s	α
3.5	0.664	5.532	0.052	0.254
4	0.582	4.731	0.021	0.207
4.5	0.526	4.162	0.009	0.169
5	0.479	3.770	0.005	0.152
5.5	0.449	3.434	0.003	0.136
6	0.434	3.158	0.002	0.120
6.5	0.426	2.937	0.001	0.112
7	0.420	2.741	0.000	0.107
7.5	0.419	2.571	0.000	0.102
8	0.471	2.412	0.000	0.089
8.5	0.473	2.286	0.000	0.083
9	0.504	2.156	0.000	0.072
9.5	0.535	2.058	0.000	0.075
10	0.615	1.958	0.000	0.058
10.5	0.689	1.869	0.000	0.045

Computational details

Complexes **1** and **2** with central symmetrical structure have one type of magnetic center Dy^{III} ion and binuclear complex **3** have two types of magnetic center Dy^{III} ions. Complete-active-space self-consistent field (CASSCF) calculations on individual Dy^{III} fragments for complexes **1**–**3** on the basis of single-crystal X-ray determined geometry have been carried out with OpenMolcas[S1] program package. Each individual Dy^{III} fragment in **1**–**3** was

calculated keeping the experimentally determined structure of the corresponding compound while replacing the neighboring Dy^{III} ion by diamagnetic Lu^{III}.

The basis sets for all atoms are atomic natural orbitals from the OpenMolcas ANO-RCC library: ANO-RCC-VTZP for Dy^{III}; VTZ for close O and N; VDZ for distant atoms. The calculations employed the second order Douglas-Kroll-Hess Hamiltonian, where scalar relativistic contractions were taken into account in the basis set and the spin-orbit couplings were handled separately in the restricted active space state interaction (RASSI-SO) procedure.[S2–S3] Active electrons in 7 active orbitals include all *f* electrons (CAS (9 in 7) in the CASSCF calculation. To exclude all the doubts, we calculated all the roots in the active space. We have mixed the maximum number of spin-free state which was possible with our hardware (all from 21 sextets, 128 from 224 quadruplets, 130 from 490 doublets for Dy^{III}. SINGLE_ANISO[S4–S6] program was used to obtain the energy levels, ***g*** tensors, magnetic axes, *et al.* based on the above CASSCF/RASSI-SO calculations.

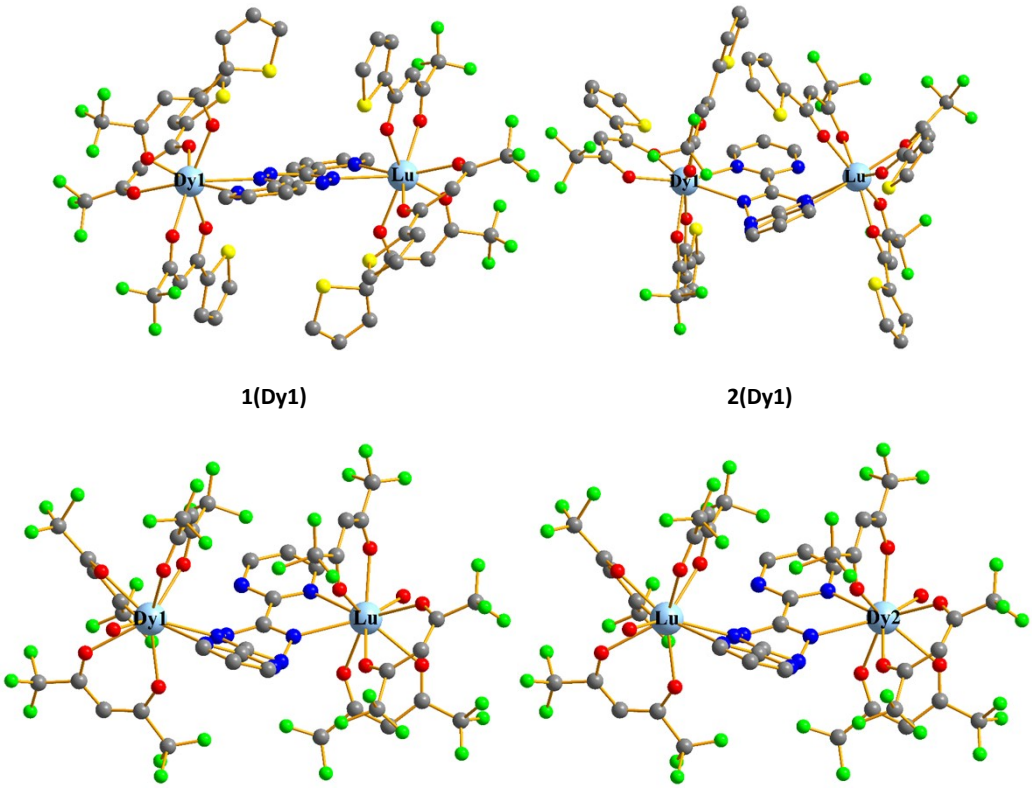

1(Dy1) **2(Dy1)**

3(Dy1) **3(Dy2)**

Fig. S38. Calculated model structures of individual Dy^{III} fragments in complexes **1**–**3**; H atoms are omitted for clarify.

Table S14. Calculated energy levels (cm^{-1}), ***g*** (g_x, g_y, g_z) tensors and predominant m_J values of the lowest eight Kramers doublets (KDs) of individual Dy^{III} fragments for complexes **1**–**3** using CASSCF/RASSI-SO with OpenMolcas.

KDs	1(Dy1)			2(Dy1)		
	E	***g***	m_J	*E*	***g***	m_J
1	0.0	0.018 0.038 19.533	±15/2	0.0	0.010 0.016 19.330	±15/2
2	125.3	0.167 0.256 16.052	±13/2	121.7	0.460 1.270 15.788	±13/2

3	173.2	1.301 1.911 12.351	±7/2	166.8	3.686 4.645 13.266	±1/2
4	210.8	8.009 5.940 3.737	±1/2	198.0	0.480 4.040 10.957	±7/2
5	263.2	2.606 3.086 12.719	±3/2	255.2	2.437 2.668 14.745	±5/2
6	370.1	0.150 0.555 17.719	±7/2	345.4	0.234 0.482 18.499	±9/2
7	436.3	0.035 0.454 15.528	±9/2	389.3	0.138 0.642 15.433	±1/2
8	479.7	0.083 0.396 17.550	±5/2	420.8	0.223 0.932 17.206	±11/2
KDs	**3(Dy1)**			**3(Dy2)**		
	E	***g***	m_J	*E*	***g***	m_J
1	0.0	0.021 0.026 19.408	±15/2	0.0	0.016 0.017 19.478	±15/2
2	122.5	1.322 1.436 16.335	±13/2	107.3	0.280 0.392 17.491	±13/2
3	171.7	10.703 7.140 3.041	±11/2	165.5	1.504 1.789 14.945	±7/2
4	185.2	0.081 2.034 13.049	±5/2	213.4	5.485 6.155 8.632	±5/2
5	232.1	2.205 2.627 14.093	±3/2	261.6	1.426 4.512 12.307	±3/2
6	255.6	1.825 2.306 14.008	±3/2	278.2	2.277 3.220 13.786	±5/2
7	283.0	0.196 1.017 14.056	±1/2	304.2	0.237 0.451 15.172	±1/2

8	329.1	0.039 0.379 17.331	±3/2	369.3	0.033 0.162 18.278	±9/2

Table S15. Wave functions with definite projection of the total moment | m_J > for the lowest eight KDs of individual Dy^{III} fragments for complexes **1**–**3**.

	E/cm^{-1}	wave functions
1(Dy1)	0.0	95.1%|±15/2>
	125.3	68.0%|±13/2>+9.5%|±11/2>+8.7%|±9/2>+4.9%|±7/2>
	173.2	19.1%|±7/2>+18.8%|±11/2>+15.1%|±3/2>+13.5%|±13/2>+13.2%|±9/2>+12.9%|±1/2>
	210.8	24.1%|±1/2>+21.6%|±11/2>+19.0%|±5/2>+15.6%|±9/2>+9.7%|±7/2>
	263.2	32.0%|±3/2>+21.2%|±5/2>+15.2%|±11/2>+11.3%|±7/2>+9.9%|±1/2>+7.8%|±9/2>
	370.1	24.4%|±7/2>+20.0%|±5/2>+19.7%|±9/2>+15.5%|±1/2>+11.0%|±11/2>
	436.3	22.7%|±9/2>+22.3%|±1/2>+19.6%|±3/2>+13.5%|±11/2>+8.5%|±7/2>+8.1%|±13/2>
	479.7	25.2%|±5/2>+22.2%|±7/2>+16.9%|±3/2>+13.7%|±1/2>+10.4%|±9/2>
2(Dy1)	0.0	90.3%|±15/2>
	121.7	47.2%|±13/2>+33.5%|±9/2>+10.0%|±11/2>
	166.8	24.5%|±1/2>+21.0%|±3/2>+16.8%|±5/2>+15.4%|±7/2>+14.7%|±13/2>
	198.0	37.0%|±7/2>+20.7%|±11/2>+15.5%|±5/2>+12.5%|±1/2>+4.3%|±13/2>
	255.2	37.0%|±5/2>+33.2%|±5/2>+11.4%|±1/2>+7.7%|±9/2>+5.7%|±7/2>
	345.4	25.5%|±9/2>+22.5%|±11/2>+19.6%|±7/2>+12.3%|±13/2>+9.6%|±5/2>
	389.3	30.3%|±1/2>+22.1%|±3/2>+14.1%|±11/2>+10.4%|±9/2>+8.0%|±5/2>+7.7%|±13/2>
	420.8	17.6%|±11/2>+16.9%|±9/2>+16.2%|±1/2>+13.4%|±7/2>+12.0%|±5/2>+11.5%|±3/2>+10.6%|±13/2>
3(Dy1)	0.0	93.9%|±15/2>
	122.5	38.2%|±13/2>22.0%|±7/2>+16.6%|±9/2>+13.3%|±11/2>
	171.7	25.3%|±11/2>+22.5%|±13/2>+16.6%|±5/2>+15.5%|±7/2>+8.9%|±9/2>
	185.2	34.1%|±5/2>+15.8%|±9/2>+15.1%|±3/2>+13.0%|±13/2>+11.5%|±11/2>
	232.1	24.5%|±3/2>+22.6%|±1/2>+15.1%|±9/2>+12.6%|±7/2>+10.5%|±5/2>+8.0%|±11/2>
	255.6	23.0%|±3/2>+22.8%|±7/2>+22.4%|±9/2>+10.6%|±5/2>+8.0%|±1/2>+6.6%|±13/2>
	283.0	41.5%|±1/2>+17.0%|±11/2>+9.2%|±5/2>+8.8%|±13/2>+8.8%|±7/2>+8.8%|±3/2>
	329.1	21.1%|±3/2>+17.8%|±1/2>+17.4%|±11/2>+17.2%|±5/2>+12.4%|±9/2>+9.4%|±7/2>
3(Dy2)	0.0	94.0%|±15/2>
	107.3	55.4%|±13/2>+23.5%|±11/2>+12.8%|±9/2>
	165.5	27.7%|±7/2>+25.6%|±9/2>+22.7%|±13/2>+11.2%|±11/2>+6.1%|±1/2>
	213.4	37.9%|±5/2>+18.5%|±11/2>+15.4%|±3/2>+9.4%|±13/2>+7.5%|±1/2>+5.4%|

		±9/2>
	261.6	28.6%|±3/2>+20.4%|±7/2>+20.4%|±1/2>+13.6%|±9/2>+7.7%|±11/2>
	278.2	26.3%|±5/2>+23.7%|±7/2>+16.9%|±3/2>+11.9%|±9/2>+10.0%|±11/2>
	304.2	46.9%|±1/2>+19.6%|±3/2>+12.1%|±5/2>+9.1%|±11/2>+5.3%|±9/2>
	369.3	24.4%|±9/2>+17.5%|±7/2>+15.9%|±11/2>+15.4%|±5/2>+14.7%|±3/2>+10.4 %|±1/2>

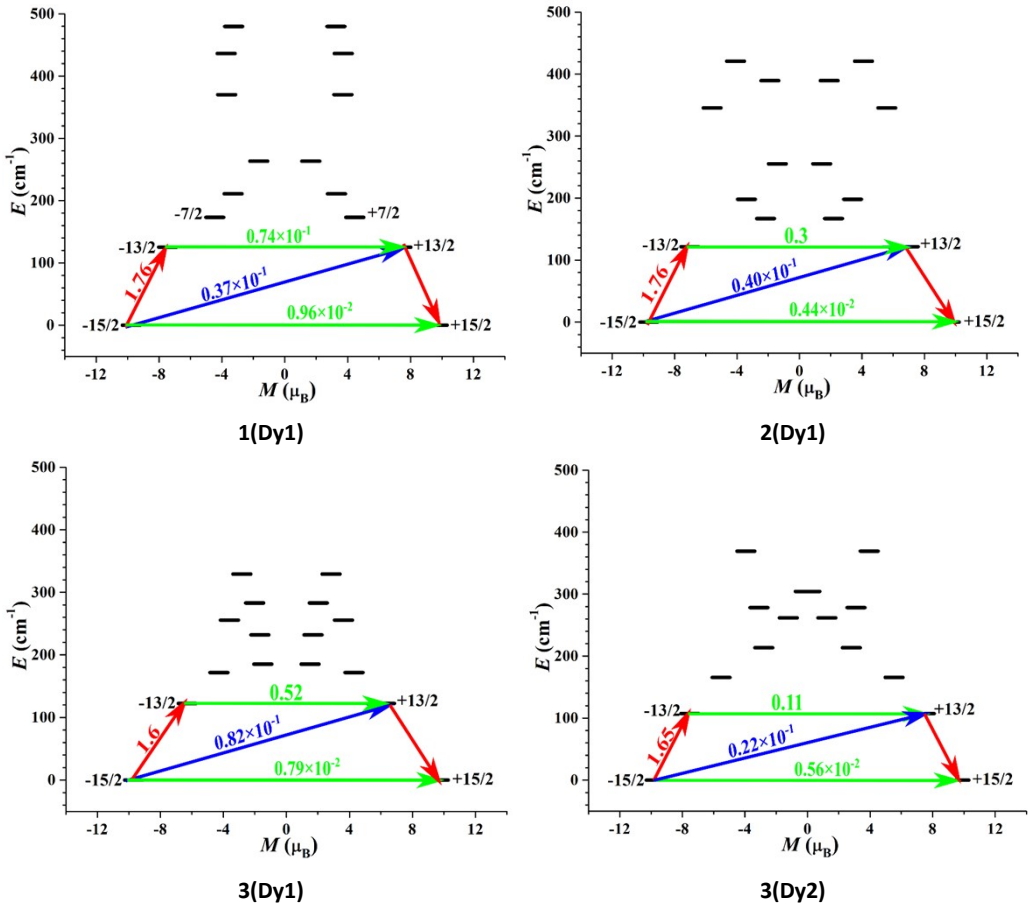

Fig. S39. Magnetization blocking barriers of individual Dy^{III} fragments for **1**–**3**. The thick black lines represent the KDs as a function of their magnetic moment along the magnetic axis. The green lines correspond to diagonal quantum tunneling of magnetization (QTM); the blue line represent off-diagonal relaxation process. The numbers at each arrow stand for the mean absolute value of the corresponding matrix element of transition magnetic moment.

To fit the exchange interactions in complexes **1**–**3**, we took two steps to obtain it. Firstly, we calculated individual Dy^{III} fragments using CASSCF/RASSI-SO to obtain the corresponding magnetic properties. Then, the exchange interaction between the magnetic centers was considered within the Lines model,[S7] while the account of the dipole-dipole magnetic coupling was treated exactly. The Lines model is effective and has been successfully used widely in the research field of *d* and *f*-elements single-molecule magnets.[S8- S9]

For complexes **1**–**3**, there is only one type of $\tilde{J}$. The Ising exchange Hamiltonian is:

$$\hat{H}_{exch} = -\tilde{J}\,\hat{\tilde{S}}_{Dy1}\,\hat{\tilde{S}}_{Dy2} \qquad \text{(S1)}$$

$\tilde{J} = 25\cos\varphi J$, where φ is the angle between the anisotropy axes on two Dy^{III} sites, and *J* is the Lines exchange coupling parameter. $\tilde{S}_{Dy}$ = 1/2 is the ground pseudospin on the Dy^{III} site. $\tilde{J}_{total}$ is the parameter of the total magnetic interaction ($\tilde{J}_{total} = \tilde{J}_{dip} + \tilde{J}_{exch}$) between magnetic center ions. The dipolar magnetic coupling can be

calculated exactly, while the exchange coupling constant was fitted through comparison of the computed and measured magnetic susceptibilities using POLY_ANISO program.[S4-S6]

Table S16. Exchange energies E (cm^{-1}), the energy difference between each exchange doublets Δ_t (cm^{-1}) and the main values of the g_z for the lowest two exchange doublets of **1**–**3**.

	1			**2**			**3**		
	E	Δ_t	g_z	E	E	g_z	E	Δ_t	g_z
1	0.000000000000	1.313×10^{-6}	1.856×10^{-9}	0.000000000000	0.92×10^{-7}	16.735	0.000000000000	5.947×10^{-7}	7.425
	0.000001313226			0.000000091944			0.000000594730		
2	0.372559744055	1.438×10^{-6}	39.066	0.292657464085	0.29×10^{-6}	34.850	0.497873861910	5.280×10^{-7}	38.171
	0.372561182459			0.292657755781			0.497874389910		

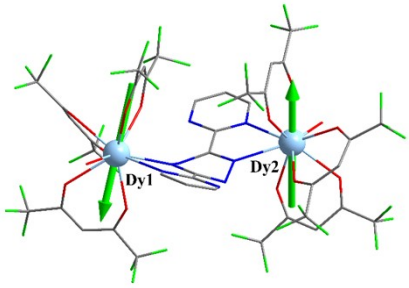

Fig. S40. Calculated orientations of the local main magnetic axes on Dy^{III} of complex **3**.

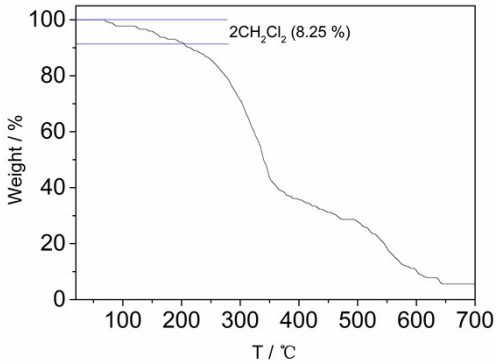

Fig. S41. The thermogravimetric analysis of complex **1**.

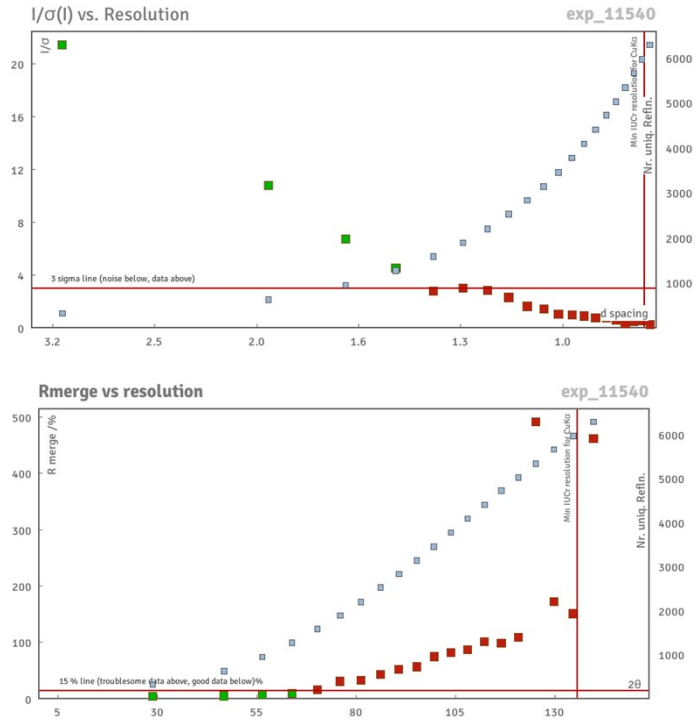

Fig. S42. The plot of I/σ vs resolution (top) and rmerge vs resolution (bottom) for complex **2**.

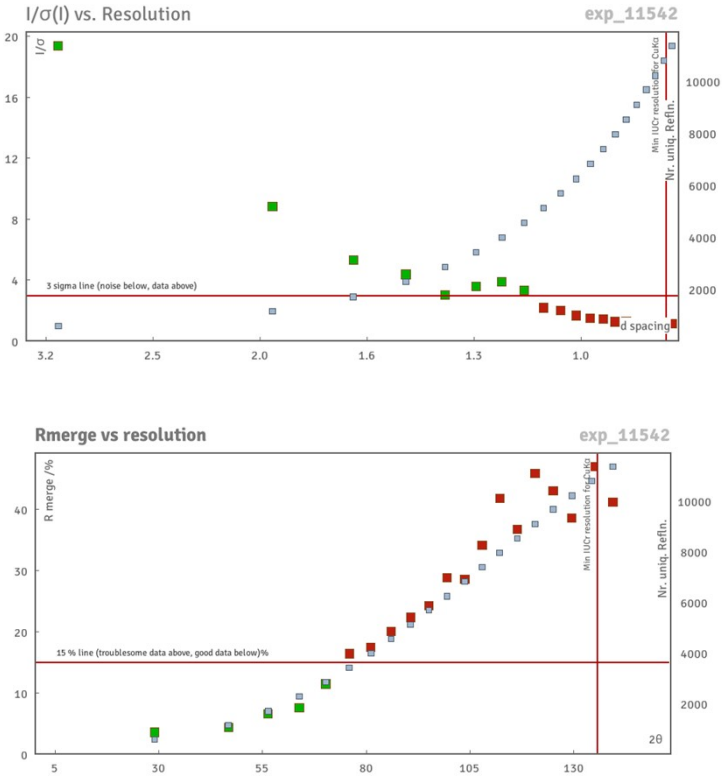

Fig. S43. The plot of I/σ vs resolution (top) and rmerge vs resolution (bottom) for complex **3**.

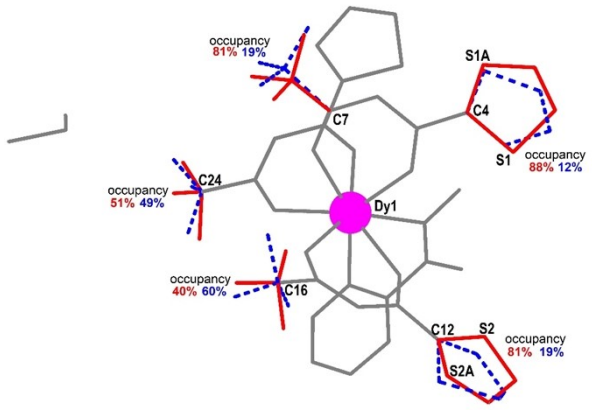

Fig. S44. Crystal structures of complex **1** show minor components of disordered structures. Atoms with 100% occupancy are shown in grey, and atoms with disordered structures are shown in colors (red and blue).

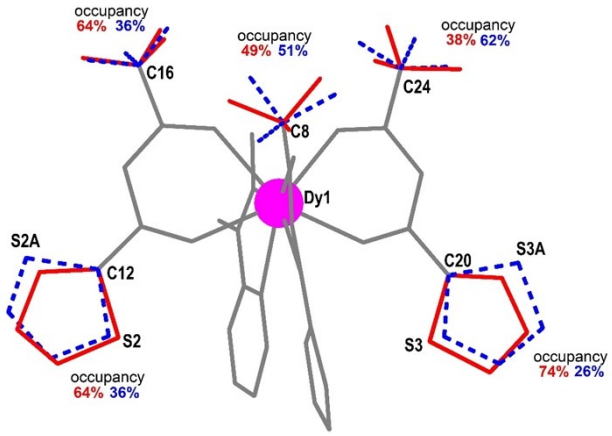

Fig. S45. Crystal structures of complex **2** show minor components of disordered structures. Atoms with 100% occupancy are shown in grey, and atoms with disordered structures are shown in colors (red and blue).

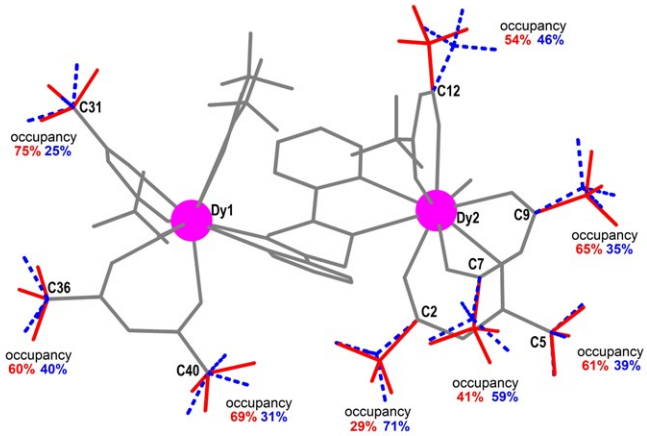

Fig. S46. Crystal structures of complex **3** show minor components of disordered structures. Atoms with 100% occupancy are shown in grey, and atoms with disordered structures are shown in colors (red and blue).

Table S17 Atomic Occupancy for complex **1**.

A tom	Occupancy	Atom	Occupancy	Atom	Occupancy
S1	0.882(7)	S1A	0.118(7)	S2	0.808(7)

S2A	0.192(7)	F1	0.81(4)	F1A	0.19(4)
F2	0.81(4)	F2A	0.19(4)	F3	0.81(4)
F3A	0.19(4)	F4	0.40(5)	F4A	0.60(5)
F5	0.40(5)	F5A	0.60(5)	F6	0.40(5)
F6A	0.60(5)	F7	0.51(4)	F7A	0.49(4)
F8	0.51(4)	F8A	0.49(4)	F9	0.51(4)
F9A	0.49(4)	C1	0.882(7)	H1	0.882(7)
C1A	0.118(7)	H1A	0.118(7)	C2	0.882(7)
H2	0.882(7)	C2A	0.118(7)	H2A	0.118(7)
C3	0.882(7)	H3	0.882(7)	C3A	0.118(7)
H3A	0.118(7)	C8A	0.19(4)	C8	0.81(4)
C9	0.808(7)	H9	0.808(7)	C9A	0.192(7)
H9A	0.192(7)	C10	0.808(7)	H10	0.808(7)
C10A	0.192(7)	H10A	0.192(7)	C11	0.808(7)
H11	0.808(7)	C11A	0.192(7)	H11A	0.192(7)

Table S18 Atomic Occupancy for complex **2**.

Atom	Occupancy	Atom	Occupancy	Atom	Occupancy
S2	0.639(15)	S3	0.737(14)	F1	0.49(5)
F2	0.49(5)	F3	0.49(5)	F4	0.64(2)
F5	0.64(2)	F6	0.64(2)	F7	0.38(3)
F8	0.38(3)	F9	0.38(3)	C9	0.639(15)
H9	0.639(15)	C10	0.639(15)	H10	0.639(15)
C11	0.639(15)	H11	0.639(15)	C17	0.737(14)
H17	0.737(14)	C18	0.737(14)	H18	0.737(14)
C19	0.737(14)	H19	0.737(14)	S3A	0.263(14)
C19A	0.263(14)	H19A	0.263(14)	C18A	0.263(14)
H18A	0.263(14)	C17A	0.263(14)	H17A	0.263(14)
S2A	0.361(15)	C11A	0.361(15)	H11A	0.361(15)
C10A	0.361(15)	H10A	0.361(15)	C9A	0.361(15)
H9A	0.361(15)	F3A	0.51(5)	F2A	0.51(5)
F1A	0.51(5)	F8A	0.62(3)	F7A	0.62(3)
F9A	0.62(3)	F6A	0.36(2)	F5A	0.36(2)
F4A	0.36(2)				

Table S19 Atomic Occupancy for complex **3**.

Atom	Occupancy	Atom	Occupancy	Atom	Occupancy

F1	0.286(12)	F2	0.286(12)	F3	0.286(12)
F4	0.614(12)	F5	0.614(12)	F6	0.614(12)
F7	0.410(14)	F8	0.410(14)	F9	0.410(14)
F10	0.653(19)	F11	0.653(19)	F12	0.653(19)
F16	0.535(17)	F17	0.535(17)	F18	0.535(17)
F25	0.753(14)	F26	0.753(14)	F27	0.753(14)
F31	0.596(13)	F32	0.596(13)	F33	0.596(13)
F34	0.694(13)	F35	0.694(13)	F36	0.694(13)
C1	0.286(12)	C6	0.410(14)	C10	0.653(19)
C11	0.535(17)	C6A	0.590(14)	F8A	0.590(14)
F7A	0.590(14)	F9A	0.590(14)	C11A	0.465(17)
F18A	0.465(17)	F16A	0.465(17)	F17A	0.465(17)
C1A	0.714(12)	F1A	0.714(12)	F2A	0.714(12)
F3A	0.714(12)	F4A	0.386(12)	F6A	0.386(12)
F5A	0.386(12)	F33A	0.404(13)	F31A	0.404(13)
F32A	0.404(13)	F36A	0.306(13)	F34A	0.306(13)
F35A	0.306(13)	F10A	0.347(19)	C10A	0.347(19)
F11A	0.347(19)	F12A	0.347(19)	F27A	0.247(14)
F25A	0.247(14)	F26A	0.247(14)		

References:

S1 Galván, I. F.; Vacher, M.; Alavi, A.; Angeli, C.; Aquilante, F.; Autschbach, J.; Bao, J. J.; Bokarev, S. I.; Bogdanov, N. A.; Carlson, R. K.; Chibotaru, L. F.; Creutzberg, J.; Dattani, N.; Delcey, M. G.; Dong, S. S.; Dreuw, A.; Freitag, L.; Frutos, L. M.; Gagliardi, L.; Gendron, F.; Giussani, A.; González, L.; Grell, G.; Guo, M. Y.; Hoyer, C. E.; Johansson, M.; Keller, S.; Knecht, S.; Kovacevic, G.; Källman, E.; Manni, G. L.; Lundberg, M.; Ma, Y. J.; Mai, S.; Malhado, J. P.; Malmqvist, P. Å.; Marquetand, P.; Mewes, S. A.; Norell, J.; Olivucci, M.; Oppel, M.; Phung, Q. M.; Pierloot, K.; Plasser, F.; Reiher, M.; Sand, A. M.; Schapiro, I.; Sharma, P.; Stein, C. J.; Sørensen, L. K.; Truhlar, D. G.; Ugandi, M.; Ungur, L.; Valentini, A.; Vancoillie, S.; Veryazov, V.; Weser, O.; Wesołowski, T. A.; Widmark, Per-Olof.; Wouters, S.; Zech, A.; Zobel, J. P.; Lindh. R. *J. Chem. Theory Comput.* **2019**, *15*, 5925–5964.

S2 Malmqvist, P. Å.; Roos, B. O.; Schimmelpfennig, B. *Chem. Phys. Lett.,* **2002**, *357*, 230–240.

S3 Heß, B. A.; Marian, C. M.; Wahlgren, U.; Gropen, O. *Chem. Phys. Lett.*, **1996**, *251*, 365–371.

S4 Chibotaru, L. F.; Ungur, L.; Soncini, A. *Angew. Chem., Int. Ed.* **2008**, *47*, 4126–4129.

S5 Ungur, L.; Van den Heuvel, W.; Chibotaru, L. F. *New J. Chem.* **2009**, *33*, 1224–1230.

S6 Chibotaru, L. F.; Ungur, L.; Aronica, C.; Elmoll, H.; Pilet, G.; Luneau, D. *J. Am. Chem. Soc.* **2008**, *130*, 12445–12455.Aquilante, F.; Autschbach, J.; Carlson, R. K.; Chibotaru, L. F.; Delcey, M. G.; De Vico, L.; Galván, I. F.; Ferré, N.; Frutos, L. M.; Gagliardi, L.; Garavelli, M.; Giussani, A.; Hoyer, C. E.; Li Manni, G.; Lischka, H.; Ma, D.; Malmqvist, P. Å.; Müller, T.; Nenov, A.; Olivucci, M.; Pedersen, T. B.; Peng, D.; Plasser, F.; Pritchard, B.;

Reiher, M.; Rivalta, I.; Schapiro, I.; Segarra-Martí, J.; Stenrup, M.; Truhlar, D. G.; Ungur, L.; Valentini, A.; Vancoillie, S.; Veryazov, V.; Vysotskiy, V. P.; Weingart, O.; Zapata, F.; Lindh, R. *J. Comput. Chem.* **2016**, *37*, 506−541.

S7 Lines, M. E. *J. Chem. Phys*. **1971**, *55*, 2977−2984.

S8 Mondal, K. C.; Sundt, A.; Lan, Y. H.; Kostakis, G. E.; Waldmann, O.; Ungur, L.; Chibotaru, L. F.; Anson, C. E.; Powell, A. K. *Angew. Chem., Int. Ed.* **2012**, *51*, 7550−7554.

S9 Langley, S. K.; Wielechowski, D. P.; Vieru, V.; Chilton, N. F.; Moubaraki, B.; Abrahams, B. F.; Chibotaru, L. F.; Murray, K. S. *Angew. Chem., Int. Ed.* **2013**, *52*, 12014–12019.